

Fracture of organosilicate glass thin films: environmental effects

J.J. Vlassak^{a,*}, Y. Lin^a, T.Y. Tsui^b

^a Division of Engineering and Applied Sciences, Harvard University, 29 Oxford Street, Cambridge, MA 02138, USA

^b Silicon Technology Development, Texas Instruments Inc., Dallas, TX 75243, USA

Received 5 May 2004; received in revised form 21 August 2004; accepted 21 August 2004

Abstract

Fracture of organosilicate glass coatings is shown to depend sensitively on reactive species in the environment: water vapor for fracture in ambient environments and hydroxyl ions for fracture in aqueous solutions. A simple model captures the key features of the experimental crack velocity curves, including the presence of a threshold energy release rate below which no crack propagation is observed and the effect of chemical species on crack velocity. The similarity between subcritical fracture of OSG in aqueous environments and results from a dissolution study suggests that both processes are controlled by the same mechanism. Bond densities obtained from both the ambient and the aqueous measurements are in line with expectations for organosilicate coatings. At high driving forces, crack growth in aqueous environments is limited by diffusion of hydroxyl ions to the crack tip.

© 2004 Elsevier B.V. All rights reserved.

Keywords: Subcritical fracture; pH; Relative humidity; Organosilicate glass; Delamination

1. Introduction

Organosilicate glass (OSG) is a leading candidate among new dielectric materials under consideration for use as interlayer dielectric (ILD) in high-performance integrated circuits. OSG is essentially silica in which some of the Si–O bonds have been replaced with bonds to organic groups, typically terminal methyl groups. As a result, OSG has a network structure similar to that of fused silica, but less dense because of the presence of the –CH₃ groups. Because of this lower density and a reduced ionic polarizability as compared to silica, OSG has a significantly lower dielectric constant. Integration of this material in a microelectronic device is not without difficulty, however, since the mechanical properties of OSG are inferior to those of silica. One important concern is the susceptibility of OSG to stress-corrosion cracking in wet environments, which may lead to failure of the device during processing.

Environmental effects on the fracture of bulk SiO₂-based materials such as amorphous silica and glass are well docu-

mented in the literature [1–6]. Recently, concerns about the reliability of integrated circuit reliability have motivated an interest in stress-corrosion cracking of thin dielectric films. The effect of moisture and temperature is well studied [7–10], but the issue of fracture and delamination of dielectric coatings in aqueous environments is only starting to be addressed [11–13]. It is well known that the dissolution rate of silica in water depends sensitively on the pH of the solution [14]. Since both dissolution and stress-corrosion cracking of silica involve rupturing Si–O bonds in the presence of reactive species, one would expect the pH of the aqueous environment to also play an important role in the subcritical fracture of silica and silica-like coatings such as OSG.

In a first section of this paper, a simple model for crack growth in the presence of a reactive species is discussed. The model is based on earlier work by Wiederhorn [3] and Lawn [2,15]. Since subcritical crack growth requires an active species to be transported to the crack tip, various transport models for both ambient and aqueous environments are briefly discussed also. In the experimental section, results of subcritical crack growth measurements in both ambient and aqueous environments will be reported for three different films stacks containing OSG films. Fracture results in

* Corresponding author. Tel.: +1 617 496 0424; fax: +1 617 496 0601.
E-mail address: vlassak@esag.harvard.edu (J.J. Vlassak).

aqueous solutions of varying pH will be discussed in light of an OSG dissolution study.

2. Model description

Environmentally aided fracture in glass and other ceramics is a complex process that can be regarded as a stress-enhanced reaction between highly strained bonds at the crack tip and a reactive species in the environment. As the driving force applied to the material increases, several regimes can be observed in which different rate limiting steps control crack growth [1,2,3,6,15]. This is illustrated in Fig. 1, which depicts a schematic graph of crack velocity versus energy release rate. At low driving forces, crack velocity is determined by the kinetics of the chemical reaction responsible for breaking bonds at the crack tip. In this regime, crack velocity increases rapidly with driving force. Often there is also a threshold energy release rate below which no crack growth is observed. In the second regime, crack velocity is limited by transport of reactants to the crack tip. In this regime, the velocity is nearly independent of the energy release rate, but depends strongly on environment. At even higher driving forces, catastrophic failure takes place and the crack velocity no longer depends on environmental factors. Simple models have been derived for each of these stages of the fracture process [1,3,6,15].

2.1. The dissolution of silica

In the reaction-controlled regime, crack velocity is determined by the rates of chemisorption of reactive species to the strained bonds at the crack tip and subsequent rupture of these bonds. This is a process that is clearly sensitive to environmental parameters. Consider for instance the case of subcritical fracture of amorphous silica under atmospheric conditions. Chemisorption of water molecules makes it easier to break the strained Si–O bonds at the crack tip allowing the crack to grow [3,16]. For subcritical crack growth in aque-

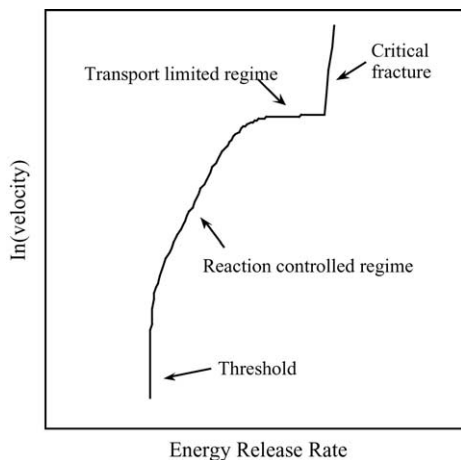
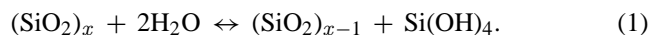
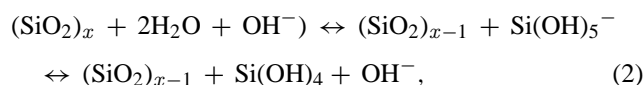


Fig. 1. Schematic graph of crack velocity vs. energy release rate.

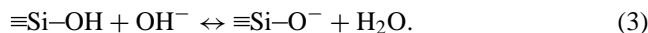
ous environments, one would expect the processes involved in the dissolution of silica in aqueous environments to provide insight in how water molecules or other reactive species such as OH^- interact with the Si–O bonds. Dissolution of silica in water is a well studied phenomenon [14,17–19] and the overall process can be represented formally by the following chemical reaction [17,19]:



The rate of dissolution depends on many factors, but generally requires a species such as OH^- or F^- that can be chemisorbed, thus increasing the coordination number of silicon atoms at the surface to more than four and weakening the oxygen bonds to underlying Si atoms. The Si atom then goes into solution as a silicate ion. Above pH 11, the silicate ion is stable, otherwise it hydrolyzes to form $\text{Si}(\text{OH})_4$ and OH^- [17]. The dissolution process can thus be written in more detail as



where the second reaction only takes place if the pH is not too high. Since the hydroxyl ion participates in the dissolution reaction, the dissolution rate is a strong function of the OH^- concentration. A slightly different mechanism was proposed more recently by Brady and Walther [14,20]. They observed that the dissolution rate of silica in alkaline environments is proportional to the surface charge of the silica and described the dissolution process in terms of deprotonation of the Si–OH groups at the surface:

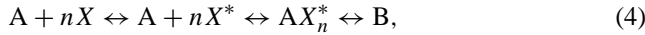


Deprotonation of the surface polarizes and weakens the underlying Si–O bonds thus promoting dissolution. Thus, the dissolution of silica is of the first order relative to the concentration of the deprotonated surface species, but not necessarily with respect to the hydroxyl ion concentration in solution. For dissolution in alkaline environments, values reported in the literature for the order relative to the aqueous OH^- concentration vary from approximately 0.3 for quartz [14] to 0.4–0.5 for amorphous silica [18]. This mechanism provides a simple explanation of the decreased dependence of the dissolution rate at very high pH through saturation of the deprotonated surface [14]. Similar dissolution mechanisms have also been presented for a number of other simple oxides and silicates [21]. Not much is known about the dissolution of organosilicate glass and how the terminal methyl groups in the structure affect the dissolution kinetics.

2.2. The reaction-controlled regime

During subcritical crack growth in a ceramic, adsorption of water or other reactive species in the environment weakens bonds near the crack tip that have already been stretched as a result of the applied load. The combined action of applied

load and chemisorbed species causes these bonds to rupture at a given rate. Several models have been developed to describe this phenomenon [1–3,6,15,22]. The following analysis is substantially based on the kink motion model by Lawn [15]. Consider crack propagation as a sequence of bond ruptures according to the following general reaction



where A represents an unbroken bond and X a reactive environmental species. X* is the chemisorbed reactive species, AX_n* the activated complex, and B represents the reaction products, i.e., the resulting broken bonds terminated in the appropriate functional groups. The Gibbs free energy change associated with Eq. (4) per unit of crack area can be calculated from the chemical potential μ of reactants and reaction products:

$$\Delta F = (\mu_B - \mu_A - n\mu_X)N = 2\gamma, \quad (5)$$

where N is the number of bonds per unit area and γ can be regarded as the surface energy of the material in the presence of the reactive species. Since energy is generally required to create new surface area, γ is positive and the energy associated with the reaction products is higher than that of the reactants. This is shown schematically in Fig. 2(a). Since the reaction in Eq. (4) is reversible, one might expect crack healing to occur in this situation [23,24]. If a load is applied, the corresponding energy release rate, G, provides a driving force for the forward reaction in Eq. (4) to occur, while making the reverse reaction more difficult. The amount of mechanical energy available per bond is G/N. Hence, when G is equal to 2γ, both reactions take place at the same rate and the crack is stationary (Fig. 2(b)); if G exceeds 2γ, the crack propagates (Fig. 2(c)).

If bond rupture is governed by Maxwell–Boltzmann statistics, the net rate at which bonds break is given by [15]

$$\omega = \omega_0 \left\{ \exp\left(-\frac{\Delta\vec{G}_0^*}{kT}\right) - \exp\left(-\frac{\Delta\overleftarrow{G}_0^*}{kT}\right) \right\}, \quad (6)$$

where ΔG₀^{*} and ΔG₀^{*}← are the activation energies for bond breaking and healing as shown in Fig. 2(a) and ω₀ ≈ kT/h

is a lattice vibration frequency. Imposition of the mechanical energy release rate changes the energy barriers to bond rupture and healing. As illustrated in Fig. 2, the energy barriers are now

$$\begin{aligned} \Delta\vec{G}^* &= \Delta\vec{G}_0^* - \frac{\beta G}{N} \quad \text{and} \\ \Delta\overleftarrow{G}^* &= \Delta\overleftarrow{G}_0^* + \frac{(1-\beta)G}{N}, \end{aligned} \quad (7)$$

provided the imposed energy release rate is not too large. Here, β is a constant reflecting the asymmetry of the energy barrier. The net rate of bond rupture is then

$$\begin{aligned} \omega &= \omega_0 \left\{ \exp\left(-\frac{\Delta\vec{G}_0^* - \beta G/N}{kT}\right) \right. \\ &\quad \left. - \exp\left(-\frac{\Delta\overleftarrow{G}_0^* + (1-\beta)G/N}{kT}\right) \right\} \\ &= \omega_0 \left[\exp\left(\frac{\beta G - \gamma}{NkT}\right) - \exp\left(-\frac{(1-\beta)G - \gamma}{NkT}\right) \right] \\ &\quad \times \exp\left(-\frac{\Delta\vec{G}_0^* + \Delta\overleftarrow{G}_0^*}{2kT}\right). \end{aligned} \quad (8)$$

If the energy barrier is symmetric, i.e., β = 1/2, the following simple relationship is found:

$$\omega = 2\omega_0 \exp\left(-\frac{\Delta G_a^*}{kT}\right) \sinh\left(\frac{G - 2\gamma}{2NkT}\right), \quad (9)$$

where ΔG_a^{*} = (ΔG₀^{*} + ΔG₀^{*}←)/2. The crack growth rate v can be found directly from Eq. (9):

$$\begin{aligned} v &= 2\omega_0 b \exp\left(-\frac{\Delta G_a^*}{kT}\right) \sinh\left(\frac{G - 2\gamma}{2NkT}\right) \\ &= v_0 \sinh\left(\frac{G - 2\gamma}{2NkT}\right), \end{aligned} \quad (10)$$

where b is the bond length and v₀ is a reference-velocity. Eq. (10) can be applied to stress-corrosion cracking in both aqueous and ambient environments. Consider the case of

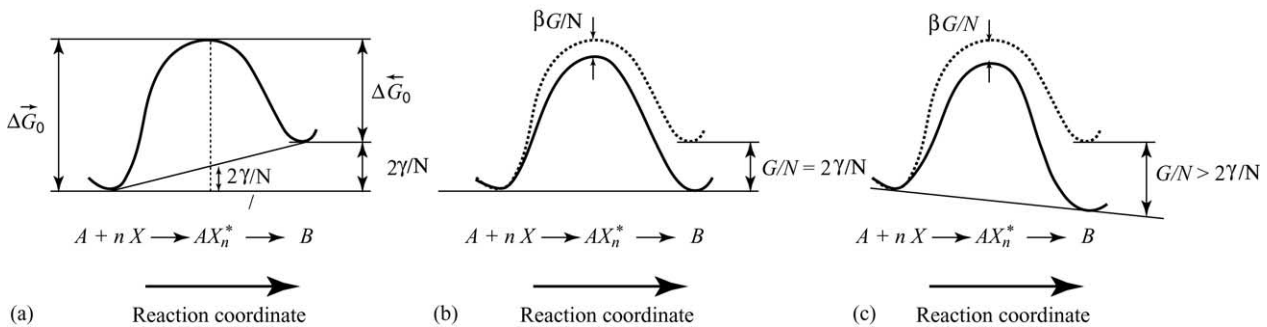


Fig. 2. Schematic graphs of the energy barriers for bond rupture: (a) G = 0, the crack heals; (b) G = 2γ, there is no net crack growth; (c) G > 2γ, the crack grows.

stress-corrosion cracking of amorphous silica or organosilicate glass. In ambient environments, the reactive species X in Eq. (4) can be identified with water, while in aqueous environments X is identified with the hydroxyl ion. Note that in this model the effect of the reactive species on crack velocity enters through the expression for 2γ given in Eq. (5), shifting the velocity curve to lower values of G with increased concentration of active species. N is the number of bonds per unit area. An alternate and more phenomenological interpretation for N is that of the inverse of an activation area for bond rupture.

2.3. The transport-controlled regime

When the driving force for crack growth increases, transport of reactive species to the crack tip becomes the rate limiting step. In this regime, crack growth rates are nearly independent of the energy release rate, but depend strongly on environment. For subcritical crack growth in ambient environments, transport of reactive species to the crack tip occurs in the gas phase. If the crack opening exceeds the mean free path of the gas molecules, flow of the ambient gas into the crack can be characterized as fluid flow. As the crack tip is approached, the crack opening decreases and the mean free path length will become larger than the crack opening at some distance from the crack tip. At this point, gas molecules more often collide with the crack faces than with other molecules and transport takes place through molecular flow [1,2]. Given the mean free path for ambient air molecules and typical crack openings for brittle solids, the transition to molecular flow occurs at a distance of approximately 1 mm from the crack tip [2]. Consequently, one would expect the molecular rather than the fluid flow regime to be rate limiting. In that case, the crack velocity is given by [1,2]:

$$v_1 = \frac{64(1 - \nu^2)Gp_X}{3\pi nNE\sqrt{2\pi m_X kT} \ln(l/b)}, \quad (11)$$

where p_X is the partial pressure of the reactive species X in the environment, m_X the molecular mass of the reactive species, l the mean free path length, and n the number of species adsorbed per bond. G the mode I energy release rate, E and ν are Young's modulus and Poisson's ratio of the solid, b the bond length. Eq. (11) describes the transport-limited crack velocity quite well as evidenced by experimental results reported in the literature [2,3,10].

The situation in liquid environments is somewhat more complicated and, as illustrated in Fig. 3, several possible transport mechanisms need to be considered. If the crack velocity is sufficiently low for the liquid to keep up with the crack, diffusion of the reactive species in the liquid may be rate limiting. If the reactive species X is assumed to diffuse to the crack tip through a stagnant boundary layer of thickness δ , a simple one-dimensional analysis shows that the corresponding crack velocity is given by

$$v_2 = \frac{bD_X}{nN\delta}([X]_\delta - [X]_c), \quad (12)$$

where $[X]_\delta$ and $[X]_c$ are the concentrations of X in the bulk of the liquid and at the crack tip, respectively. If diffusion of X is rate limiting, X chemisorbs as soon as it reaches the crack tip and $[X]_c$ approaches zero. The salient feature of Eq. (12) is then that the limiting crack velocity is linearly proportional with the concentration of X in the liquid. Note that depending on the concentration of X , it may be necessary to write Eq. (12) in terms of the activity of X in the liquid.

There is experimental evidence that flow of the liquid to the crack tip can be rate limiting for cracks moving at high velocities [6,25]. In the vicinity of the crack tip, the crack has a parabolic profile described by [26]

$$u = 2\sqrt{\frac{2G(1 - \nu^2)}{\pi E}}\sqrt{x}. \quad (13)$$

Here, x is the distance from the crack tip. If the crack moves at a velocity v_3 , the total flow through a plane perpendicular to the direction of propagation and at a distance x from the crack tip is

$$F = 2uv_3 = 4v_3\sqrt{\frac{2G(1 - \nu^2)}{\pi E}}\sqrt{x}, \quad (14)$$

where F is defined as flow per unit width. For laminar flow of a fluid with viscosity μ through a channel of width $2u$, one has

$$\frac{dp}{dx} = \frac{3F\mu}{2u^3} = \frac{3\pi\mu v_3 E}{8G(1 - \nu^2)x}, \quad (15)$$

taking into account Eqs. (13) and (14). Integrating Eq. (15) provides the following expression for the pressure at a distance x of the crack tip

$$p(x) = p_a - \frac{3\pi\mu v_3 E}{8G(1 - \nu^2)} \ln\left(\frac{c}{x}\right), \quad (16)$$

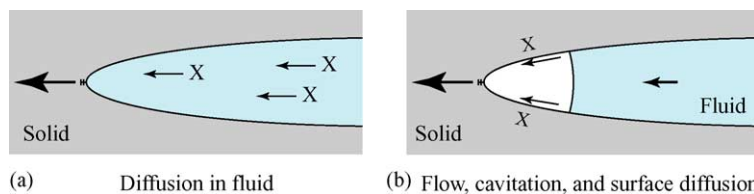


Fig. 3. Possible limiting transport mechanisms in aqueous environments: (a) diffusion of active species in fluid; (b) cavitation of fluid near crack tip. The active species may in the latter case still reach the crack tip through surface diffusion along the crack faces.

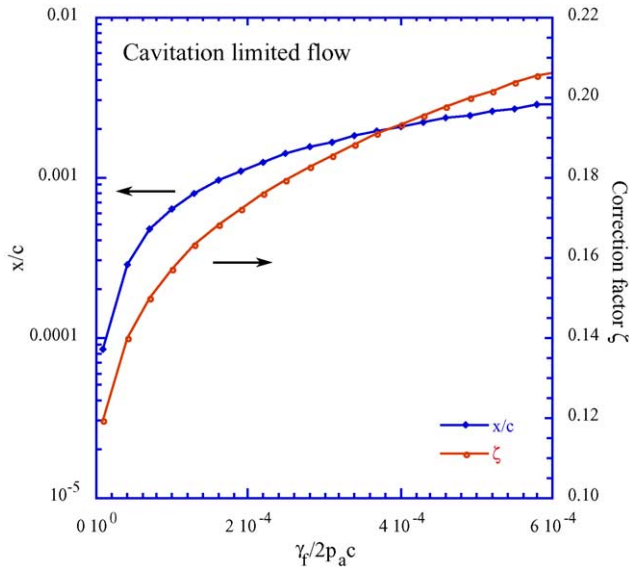


Fig. 4. Variation of cavitation bubble size and correction factor ζ with the dimensionless parameter $\gamma_f/2p_a c$.

where c is the crack length and p_a the ambient fluid pressure. The pressure $p(x)$ in Eq. (16) has a lower limit determined by cavitation of the fluid [25]. Assume a bubble with radius of curvature R forms at the crack tip as depicted in Fig. 3. The pressure in the fluid required to maintain the bubble is

$$p = -\frac{\gamma_f}{R}, \quad (17)$$

if the curvature of the bubble along the crack front is small and the fluid vapor pressure inside the bubble is neglected. In this expression, γ_f is the surface tension of the fluid. Assuming further that the bubble intersects the crack faces at right angles at a distance x from the crack tip, the radius is found to be

$$R \approx u \left(\frac{du}{dx} \right)^{-1} = 2x. \quad (18)$$

Eq. (18) is easily modified if the contact angle is different from 90° . Combining Eqs. (16)–(18) yields an expression for the crack velocity in terms of x

$$v_3 = \frac{8G(1-v^2)p_a}{3\pi\mu E \ln(c/x)} \left(1 + \frac{\gamma_f}{2p_a c} \left(\frac{c}{x} \right) \right). \quad (19)$$

This is the maximum velocity the crack can attain before a bubble may form at the crack tip. This limiting velocity depends on x and hence on the size of the bubble formed at the crack tip. The minimum velocity for which bubble formation can occur is found by minimizing v_3 with respect to x :

$$v_3 = \zeta \frac{8G(1-v^2)p_a}{3\pi\mu E}, \quad (20)$$

where ζ is a numerical constant that depends on the dimensionless parameter $\gamma_f/2p_a c$. At velocities below v_3 , the pressure in the crack is not low enough anywhere in the crack to sustain a bubble. Fig. 4 shows how ζ and bubble size

vary with $\gamma_f/2p_a c$. If the wetting angle is different from 90° , the relevant dimensionless parameter is also a function of the wetting angle, the elastic stiffness of the material, and the applied energy release rate, but the results are qualitatively very similar. It should be emphasized that v_3 is the minimum velocity at which a stable bubble can form. If nucleation of a bubble of sufficient size is difficult, larger velocities are required. It should be noted that even if a bubble forms at the crack tip as depicted in Fig. 3, it may still be possible for the reactive species to reach the crack tip by means of surface diffusion or through formation of a precursor film for wetting liquids [27]. If so, the velocity of the crack is determined by a combination of fluid flow and surface diffusion. If the crack faces are rough, flow into the crack is hindered and the crack velocity at which fluid flow is rate limiting is reduced. It is therefore desirable to determine the effect of roughness on flow of the fluid to the crack tip. A simple model to account for this effect is presented in Appendix A. According to this model, Eq. (16) needs to be replaced by

$$p(x) = p_a - \frac{3\pi\mu v_3 E}{8G(1-v^2)} \int_x^c \frac{1}{x\rho(\lambda)} dx, \quad (21)$$

where $\rho(\lambda)$ is a correction factor that depends on the roughness of the crack faces, the crack opening displacement, and the amount of mode II versus mode I loading of the crack. The exact definition of $\rho(\lambda)$ can be found in Appendix A. In general, the integral in Eq. (21) needs to be evaluated numerically. The effect of roughness is relatively small in most cases.

3. Experimental methods

Subcritical delamination experiments were conducted on film stacks containing organosilicate coatings and three types of capping layers. To this effect, (100)-Si substrates were coated at 400°C with 500 nm organosilicate (OSG) films using an industrial plasma enhanced chemical vapor deposition process (PECVD) with oxygen and 3,5,7-tetramethylcyclotetrasiloxane (TMCTS) as precursors. The OSG films were capped with three different barrier layers: 80 nm of SiN_x , 30 nm of TaN, and 250 nm of SiO_2 . The SiN_x and SiO_2 coatings were deposited using PECVD processes. The precursors for the SiN_x coatings were SiH_4 , N_2 and NH_3 , while the precursor for the SiO_2 coatings was tetraethoxysilane (TEOS) [28]. The TaN coatings were deposited using reactive sputtering from a Ta target. The precise film stacks are summarized in Table 1.

Table 1
Film stack information

Materials system	Film stack
OSG/TaN	500 nm OSG/30 nm TaN/150 nm Cu
OSG/ SiN_x	500 nm OSG/80 nm SiN_x /40 nm Ti/400 nm Cu
OSG/ SiO_2	500 nm OSG/250 nm SiO_2 /40 nm Ti/400 nm Cu

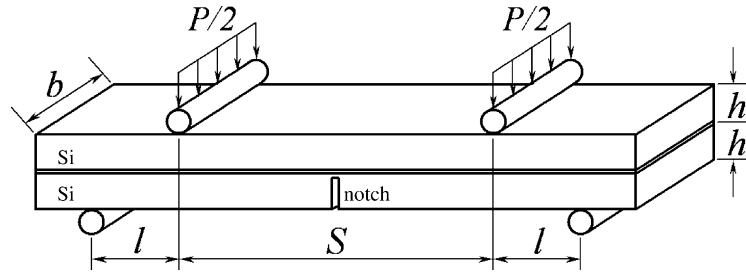


Fig. 5. Schematic representation of the specimen configuration in the four-point bend test.

Subcritical delamination experiments were performed using the four-point bending technique. Test specimens were prepared by bonding SiN_x -coated Si wafers to the substrates with the film stacks of interest using a spin-on epoxy (EPO-TEK 353ND). The epoxy was cured at 90°C for 60 min under a pressure of 8 kPa. The epoxy thickness after the curing cycle was approximately $5\ \mu\text{m}$. In order to increase the distance between the film stack and the epoxy, 40 nm of Ti and 400 nm of Cu were sputter deposited onto the SiO_2 and SiN_x samples prior to spin-coating the epoxy. The TaN samples were coated with 150 nm of Cu. After bonding, the sandwiched structures were diced into $60\ \text{mm} \times 6\ \text{mm}$ specimens. Finally, a notch was machined to within approximately $30\ \mu\text{m}$ of the interface using a high-speed dicing saw. Small variations in the adhesion or fracture toughness of coatings deposited at different instants of time are quite common. In order to minimize these changes, all specimens for a given set of experiments were prepared at the same time and randomized with respect to the experimental conditions.

Fig. 5 is a schematic representation of the specimen configuration in the four-point bending test. As the specimen is loaded in pure bending, a crack emanates from the notch and propagates along the weakest interface in the film stack. The energy release rate G at the crack tip can be expressed as [29,30]

$$G = \frac{21P^2l^2(1-\nu^2)}{16Eb^2h^3}, \quad (22)$$

where E and ν are the elastic modulus and Poisson's ratio of the Si substrate, P is the load, l the distance between the inner and outer loading pins, b the width of the specimen, and h the substrate thickness. This specimen configuration results in mixed-mode loading with a macroscopic loading phase angle of approximately 41° [31]. During crack propagation, the compliance of the beam is a function of the crack length. Hence, the crack growth rate v can be evaluated from the rate of change of the sample compliance and is given by the following equation [32]

$$v = \frac{8Eb^2h^3}{21(1-\nu^2)l^2} \frac{d}{dt} \left(\frac{H}{P} \right), \quad (23)$$

where H is the deflection of the beam. The crack growth rate in Eq. (23) is the rate of change of the total crack length. Experimentally, it is observed that the crack does not grow symmetrically with respect to the center of the sample. Usu-

ally, only one crack grows while the other is stationary. Hence, the crack growth rate in Eq. (23) represents the velocity of a single crack.

Crack growth rates were measured as a function of applied energy release rate using a load relaxation technique with constant displacements [32]. All measurements were made using the following two-step method: first, samples are preloaded in a shortened- S configuration until delamination occurs, where S is the span between the two inner loading pins ($S = 12\ \text{mm}$). The plateau load at which the crack propagates along the interface is used to determine the critical energy release rate for delamination. Next, the samples are unloaded and the spacing between the inner loading pins is increased to 36 mm. After reloading the samples to a predetermined load, the displacement is held constant and the load is recorded as the crack continues to grow. Eqs. (22) and (23) are used to derive crack velocity as a function of applied energy release rate. All measurements were conducted using a custom-built, high-stiffness, low-drift, four-point bending test system with in situ environmental cell. A load cell of the metal-foil type and with a resolution of 10 mN (Sensotec 31) was selected to minimize drift effects. Throughout all loading steps, the displacement rate was held constant at $0.5\ \mu\text{m/s}$. All experiments were conducted at 26°C and the total temperature drift was less than 1°C over a period of 24 h. To minimize the effect of vibrations on the measurements, the entire test assembly was placed on a vibration isolation table.

The environmental cell can run in both ambient and aqueous modes. In the ambient mode, the cell provides a N_2 or a N_2/O_2 atmosphere with precise control over the relative humidity in the chamber, while the aqueous mode makes it possible to perform measurements in buffer solutions of a given pH. The accuracy of the relative humidity values is approximately 2%. In this study, aqueous solutions were prepared from HCl, KCl, and KOH solutions. The desired pH values were obtained by titration. The KCl solution was used to maintain a constant Cl^- concentration of 0.122 M. All pH values were measured using a FUTURATM pH electrode from BECKMAN. Before each measurement, the electrode was calibrated using standard pH buffer solutions provided by VWR. The measured pH values are accurate to ± 0.1 pH unit.

After delamination, the fractured specimens were carefully opened and analyzed using X-ray photoelectron spectroscopy (XPS) to determine the crack path in the thin film

stacks. All measurements were made with Al K α radiation using a Surface Science XPS system, model SSX-100. Information thus obtained comes from the first 20 Å of material in the sample. Composition depth profiles were obtained by making XPS measurements after eroding the surface of the samples with a 4 keV Ar⁺ ion beam at an incident angle of 45°.

In order to determine the morphology and roughness of the crack faces, fractured surfaces were also investigated with atomic force microscopy (AFM) using a Dimension 3100 Scanning Probe Microscope from Veeco equipped with a tapping mode tip from Pacific Nanotechnology. AFM images for the OSG/SiN_x, OSG/SiO₂, and OSG/TaN materials systems were obtained by scanning several 1000 nm × 1000 nm areas in the immediate vicinity of the crack tip. Both fracture surfaces obtained in air and in aqueous environment were examined.

In addition to the subcritical delamination experiments in various ambient and aqueous environments, the dissolution rate of OSG films was measured as a function of pH. Experiments were conducted over a pH range from 6 to 13. Aqueous solutions with a Cl⁻ concentration of 0.12 M were prepared from HCl, KCl, and KOH solutions. The pH of the solutions was measured using a FUTURATM pH electrode. For each pH value, two Si substrates with 0.5 μm OSG coatings were enclosed in a sealed Teflon frame so that only the OSG films were exposed to the solution. The total area in contact with the buffer solution was 20.25 cm² for each specimen. The frames with the OSG films were placed in 3.8 × 10³ cm³ of buffer solution in sealed polyethylene reaction vessels. The vessels were placed in a water bath with a constant temperature of 22.0 ± 0.1 °C. There was no agitation during the dissolution experiments. The duration of the dissolution experiments was 270 h. To determine the etch rate, film thickness measurements were made at regular time intervals using a V-VASE Spectroscopic Ellipsometer from J.A. Woollam Co., Inc. Each time, thickness measurements were made at three predefined locations on the samples. Since the OSG films are amorphous, dissolution of the films proceeds in a uniform fashion. Thus, thickness changes provide a good indication of the total amount of material dissolved and there is no need to track the composition of the buffer solutions. After each experiment, the pH of the solution was measured. In all cases, only a small change in pH was detected over a 270 h period. For the near-neutral solutions the change was less than one pH unit, while for the alkaline solutions the change was as small as 0.2 pH units. The total amount of Si dissolved in the most alkaline solution corresponds to a Si concentration in the buffer solution of approximately 0.1 ppm. This is an insignificant fraction of the saturation concentration of amorphous silica. While it is not known how the organic groups in the OSG films affect its solubility, the OSG film thickness decreased linearly in time indicating that no significant back reaction occurred and that the dissolution experiments were conducted far from saturation conditions.

4. Results

Fig. 6 summarizes the results from the dissolution study in a plot of dissolution rate as a function of pH. For comparison, the dissolution rates of amorphous silica as reported in the literature is also shown. Dissolution rates were determined from linear least squares fits to the OSG film thickness as a function of time. In some dissolution studies of amorphous silica, two reaction regimes are observed [18]. Initially, there is a regime during which the amount of Si in solution increases parabolically. This regime is followed by a linear regime, where the Si concentration increases linearly with time. The parabolic regime has been attributed to the presence of flaws in the surface of the silica or to diffusion of water into the silica and release of weakly bonded silica tetrahedra [18]. In the present experiments, only a linear dissolution regime was observed. While one might expect OSG and amorphous silica to have similar chemical properties, the absence of a parabolic regime is not entirely surprising given that the dissolution rate in this study was determined from the change in film thickness, rather than from the composition of the solvent. As illustrated in Fig. 6, the logarithm of the dissolution rate changes linearly with pH in a range of 6–13 and the slope is 0.53 ± 0.04. Consequently, the dissolution of OSG follows a power law in the OH⁻ concentration with exponent 0.53 ± 0.04.

Fig. 7(a) shows typical XPS spectra for an OSG/TaN sample delaminated in air at a relative humidity of 50%. One of the fracture surfaces consists of OSG as indicated by the presence of Si, C, and O signals, but the character of the other surface is not as clear. After 60 s of Ar⁺ sputtering, however, peaks for Ta and N become evident. Delamination therefore occurs within the OSG layer, parallel to the TaN/OSG interface. The thickness of the OSG remaining on the TaN side is estimated from the time required to remove it by

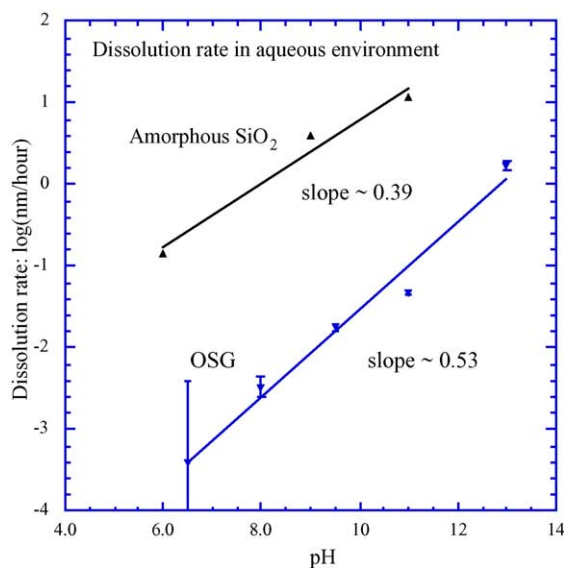


Fig. 6. Dissolution rate of OSG and amorphous silica as a function of pH. Data for amorphous silica is from Wirth and Gieskes [34].

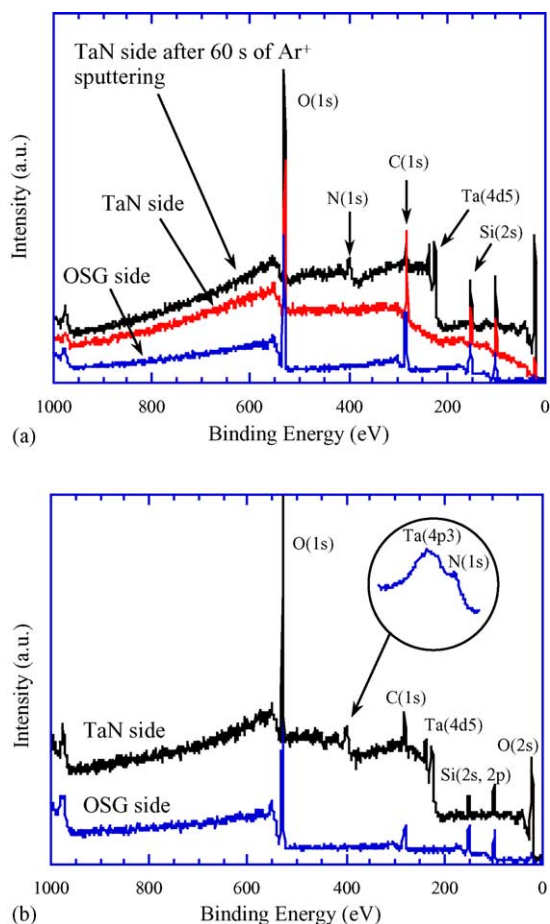


Fig. 7. (a) Typical XPS spectra for an OSG/TaN sample delaminated (a) in air at a relative humidity of 50% and (b) in water at pH 7.

sputtering to be approximately 5 nm. XPS spectra for an OSG/TaN sample delaminated in an aqueous environment with pH 7 are depicted in Fig. 7(b). Unlike for specimens delaminated in air, the crack faces on the TaN side of these samples show signals for Ta and N, without ion sputtering. Since the escape depth of photoelectrons is approximately 2 nm, one can expect the thickness of the residual OSG layer on the TaN surface to be less than 2 nm. Fig. 8 shows an AFM image of a crack face on the TaN side for a specimen delaminated in a pH 13 buffer solution. This image clearly illustrates that that crack face is quite smooth with an RMS roughness on the order of 0.98 nm. This observation supports a mechanism where the crack propagates very near the OSG/TaN interface allowing some photoelectrons originating in the TaN to escape and occasionally exposing the underlying TaN. It may be somewhat surprising that a crack would propagate within the OSG layer rather than at the interface for a specimen subjected to mixed-mode loading. Because the OSG film is much more compliant than the Si substrate, an elasticity analysis [31] shows that the crack will be trapped within the compliant layer even for mixed-mode loading. Since the mode II loading component is significant, the crack will not propagate in the center of the film, but close to the interface. The

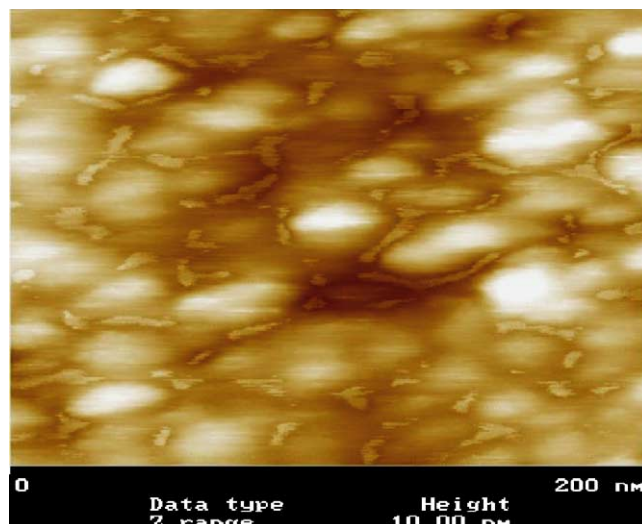


Fig. 8. AFM image of a crack face on the TaN side for a specimen delaminated in a pH 13 buffer solution.

surface topography of the crack faces as shown in Fig. 8 has a characteristic wavelength of about 30–40 nm. The precise origin of this pattern is not known, but may be related to inhomogeneity in the OSG at this length scale. Célerié et al. [33] recently reported the formation of cavities ahead of a crack tip in glass subjected to stress-corrosion. The length scale of these voids is similar to the roughness observed in the OSG experiments in this study. Finally, it should be pointed out that some OSG may dissolve in the buffer solution during the delamination experiments reducing the amount of OSG on the TaN. Results of the dissolution rate experiments, however, lead to the conclusion that on the time scale of the delamination experiments, dissolution plays a role only in the most alkaline solution.

Fig. 9(a) and (b) depict XPS spectra for OSG/SiN_x samples delaminated in air with a relative humidity of 50% and in a buffer solution with pH 7, respectively. The XPS spectra for both crack faces are similar and are distinguished mainly by the N(1s) signal at 397.3 eV on the SiN_x side. The spectra for delamination in ambient or aqueous conditions are comparable and indicate that delamination occurred at or very near the OSG/SiN_x interface in both cases. Since the N(1s) signal for the specimen delaminated under ambient conditions is relatively weak compared to that delaminated in aqueous environment and given the presence of the C and O peaks, more OSG remains on the SiN_x side after delamination under ambient than under aqueous conditions. AFM images show that the crack faces are quite smooth with an RMS roughness of approximately 1 nm and with no significant difference between the aqueous and ambient specimens. Based on the XPS and AFM results, one can conclude that the crack propagates within the OSG only a short distance from the interface and occasionally exposing SiN_x.

The interpretation of the XPS spectra for the OSG/SiO₂ sample shown in Fig. 10 is not as straightforward. Analysis

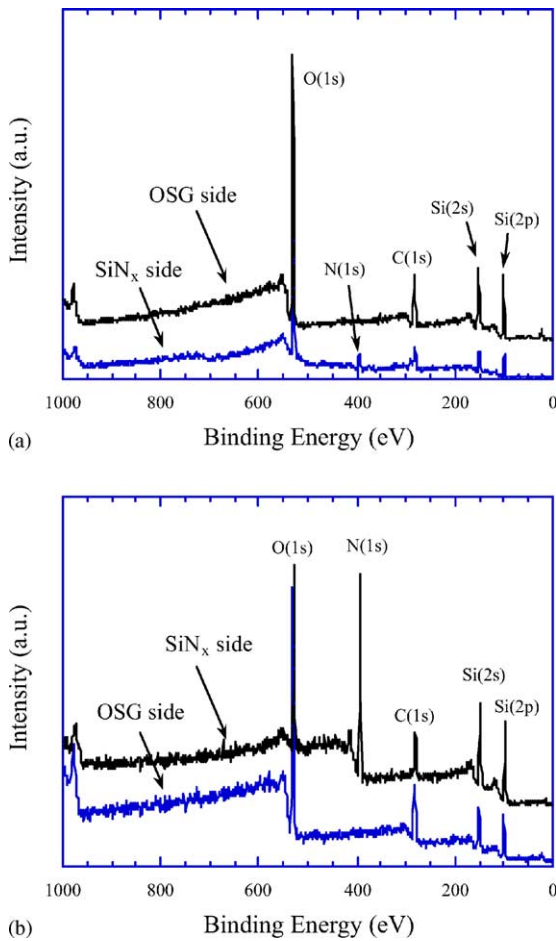


Fig. 9. Typical XPS spectra for OSG/SiN_x samples delaminated (a) in air with a relative humidity of 50% and (b) in an aqueous buffer solution of pH 7.

of both fracture surfaces results in very similar spectra, even after 60 s of Ar⁺ sputtering to remove any adsorbed hydrocarbons. Since TEOS-based SiO₂ contains a certain amount of carbon, it was necessary to perform an XPS analysis of blanket films of SiO₂ and OSG in order to identify the crack

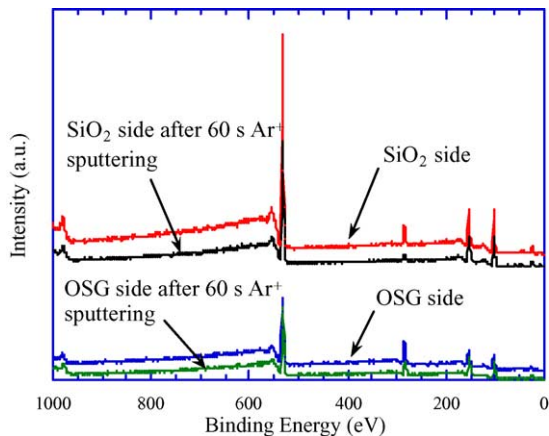


Fig. 10. Typical XPS spectra for an OSG/SiO₂ sample delaminated in air with a relative humidity of 50%.

Table 2

Composition of the crack faces of an OSG/SiO₂ sample and blanket TEOS PECVD SiO₂ and OSG films, before and after Ar sputtering (sputtering was performed for 60 s with an energy of 4 keV)

Surfaces	O (at.%)	C (at.%)	Si (at.%)
SiO ₂ side	53	16	31
SiO ₂ side (after sputtering)	54	10	36
Blanket SiO ₂	54	15	31
Blanket SiO ₂ (after sputtering)	55	9	36
OSG side	43	31	26
OSG side (after sputtering)	44	19	37
Blanket OSG	47	29	24
Blanket OSG (after sputtering)	42	20	38

path. A comparison of the composition of the fracture surfaces before and after Ar⁺ sputtering (see Table 2) clearly indicates that one surface consists of OSG, while the other of TEOS-based SiO₂. Hence, delamination for this materials system takes place at the OSG/SiO₂ interface. AFM scans show again very smooth crack faces with an RMS roughness of less than 1 nm for both aqueous and ambient specimens.

Fig. 11 shows subcritical crack growth data for the three materials systems in an ambient environment with controlled relative humidity. For the purpose of clarity, only one representative curve for each humidity condition is shown, although at least four specimens were tested for each value of relative humidity. The curves in Fig. 11 are all similar indicating that subcritical delamination in these systems is controlled by the same mechanism. With increasing relative humidity, the stress-corrosion thresholds shift to lower values of the energy release rate. Fig. 12 shows the threshold energy release rate as a function of the natural logarithm of the water partial pressure in the environment. The reproducibility of the measurements is quite good as witnessed by the error bars in the figure, which correspond to one standard deviation of the measurement population at a given relative humidity level. The figure illustrates clearly that there is a linear relationship between threshold energy release rate and the logarithm of the pressure.

Fig. 13 shows subcritical crack growth curves for the OSG/SiO₂ system in various pH buffer solutions and compares them to data obtained in ambient environments with different levels of relative humidity. For a given crack velocity, there is a clear progression towards lower energy release rates as the relative humidity in the air increases, or as the pH increases for the aqueous environments, with energy release rates approximately the same for very humid environments or acidic solutions. At a given energy release rate, the crack velocity can differ by many orders of magnitude depending on the pH of the buffer solution. Representative subcritical crack growth curves for both the OSG/TaN and OSG/SiN_x system are shown in Fig. 14(a) and (b). The specimens used to obtain these results were fabricated at a different time than those used for the ambient measurements. Since there is a small shift in fracture toughness for these specimens, the results from these specimens cannot be directly compared with the ambient measurements. The results in Fig. 14 show

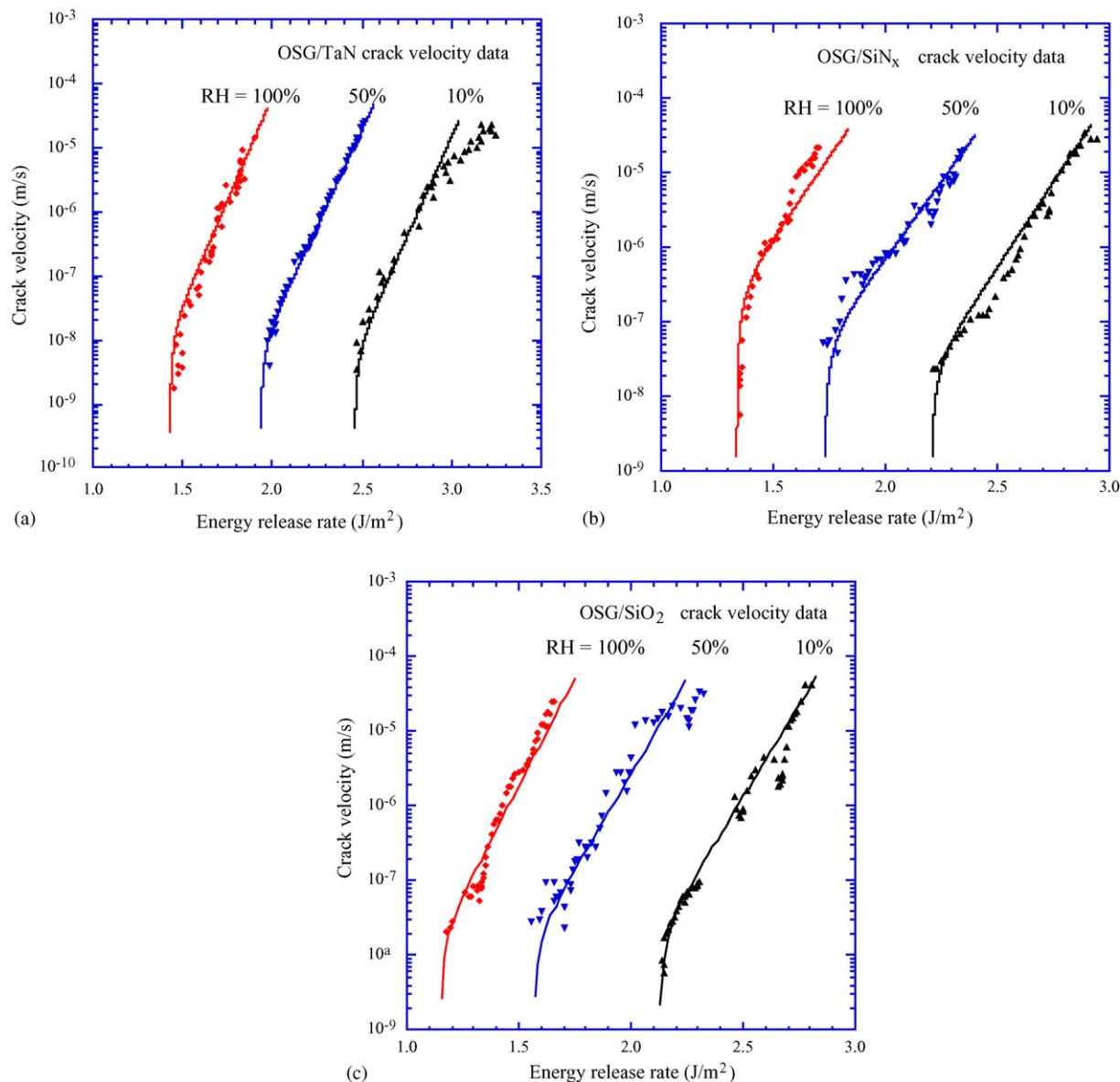


Fig. 11. Representative subcritical crack growth curves in ambient environment for (a) the OSG/TaN system, (b) the OSG/SiN_x system, and (c) the OSG/SiO₂ system. Solid symbols represent experimental measurements; curves are fits to the experimental results using Eq. (10).

that pH has a significant effect on the crack growth rate in the films. The pH of the aqueous solution also changes the threshold energy release rate for both systems. The threshold energy release rate is plotted as a function of pH for the three materials systems in Fig. 15. Again, a linear relationship is obtained with a slope that is approximately the same for all three materials systems.

5. Discussion

5.1. OSG dissolution results

Fig. 6 shows the OSG dissolution rate constant as a function of pH and compares it to the dissolution rate of amor-

phous silica. In both cases, the dissolution rate increases dramatically with increasing pH. This observation is consistent with results obtained for a wide range of silica-containing minerals [14,18,20]. Brady and Walther [14] have developed a model for the dissolution of silicates in which the dissolution rate has a first order dependence on the concentration of a reactive species on the surface of the silicate, i.e., the deprotonated Si–OH surface groups in this case. This model yields a similar pH dependence for all silica-containing minerals in alkaline environments: if k represents the dissolution rate constant, then $\partial \log k / \partial \text{pH}$ takes on values around 0.3. The dissolution rate data for amorphous silica shown in Fig. 6 yield a $\partial \log k / \partial \text{pH}$ of approximately 0.39, while results from a study by Mazer and Walther [18] suggest a value of 0.4–0.5, where the higher value applies to the linear reaction regime.

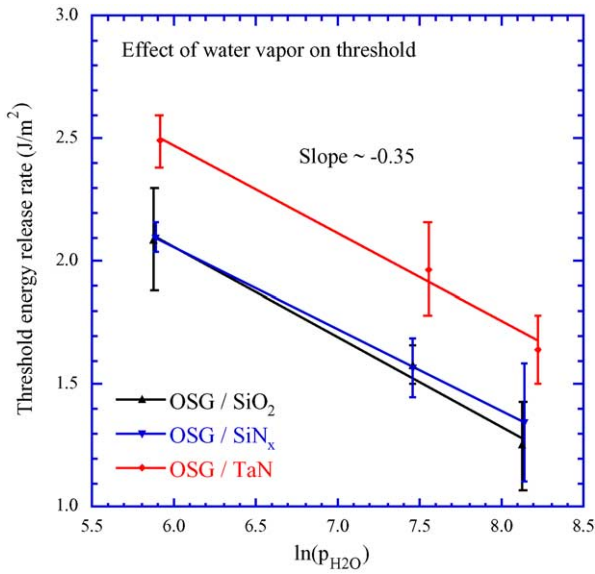


Fig. 12. Threshold energy release rate vs. partial pressure of the water vapor for delamination in ambient environments. The water partial pressure is given in Pa.

The value obtained for OSG is 0.53 ± 0.04 , in good agreement with the results for amorphous silica. This observation implies that the dissolution mechanisms for amorphous silica and OSG are similar and suggests that the appropriate value for n in Eqs. (4) and (5) is 0.53 ± 0.04 , when applied to OSG in alkaline environments. The dissolution of OSG is significantly slower than that of amorphous silica. This is somewhat surprising since OSG has a more open structure than amorphous silica and dissolution of OSG requires fewer Si–O bonds to be severed. Indeed, Rutherford back scattering (RBS) measurements performed on the OSG films [35] show that on average each Si atom is bonded to a methyl group and three oxygen atoms. The terminal methyl groups

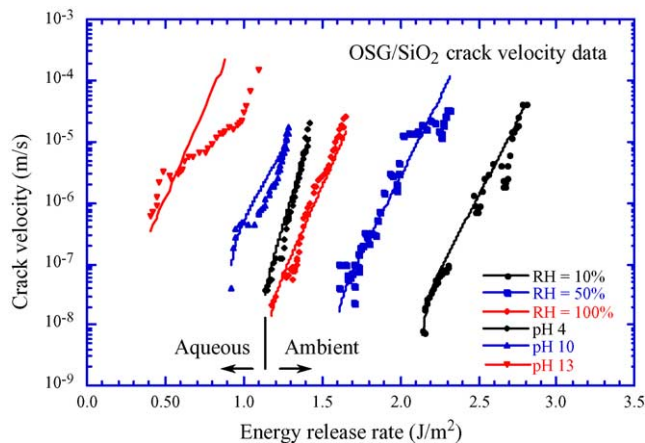


Fig. 13. Representative crack growth curves for the OSG/SiO₂ system in aqueous solutions of various pH and in ambient environments with different levels of relative humidity. Solid symbols represent experimental measurements; solid lines are curve fits.

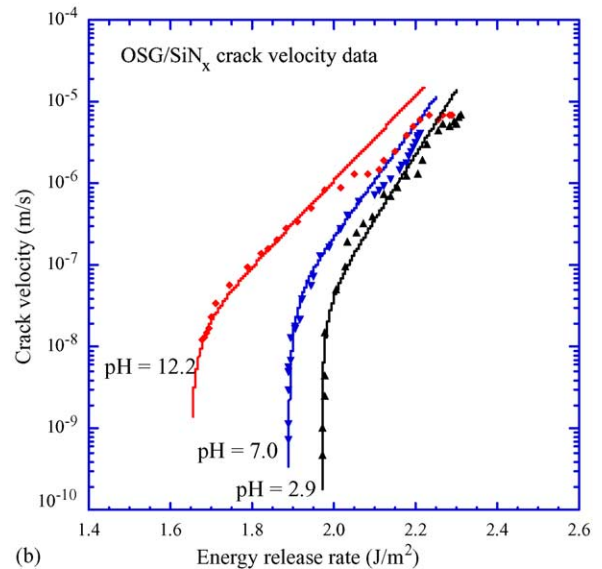
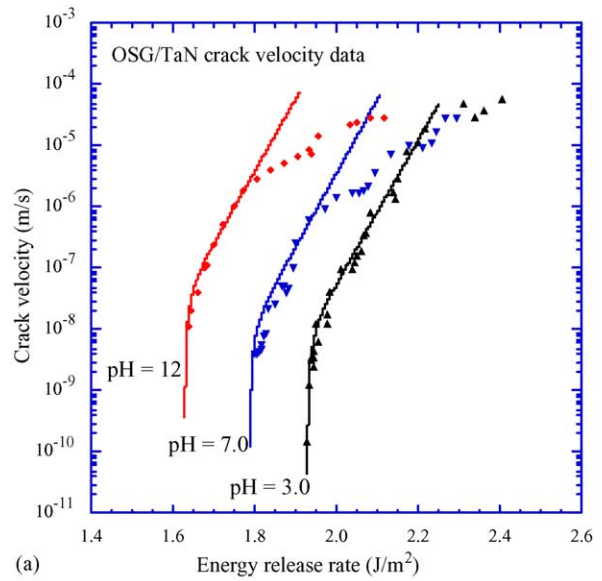


Fig. 14. Representative subcritical crack growth curves in aqueous environment for: (a) the OSG/TaN system and (b) the OSG/SiN_x system. Solid symbols represent experimental measurements; curves are fits to the experimental results using Eq. (10).

in the OSG structure apparently provide enough steric hinder to compensate for this reduced number of bonds. Note that the OSG composition as listed in Table 2 does not necessarily give the correct ratios of C to O in the OSG films since differential sputtering of C and O atoms may skew the results.

5.2. Effect of water vapor on subcritical fracture of OSG

The XPS results combined with the AFM images indicate that upon delamination in ambient environments, the crack propagates within the OSG film for the OSG/TaN and OSG/SiN_x samples and at the interface for the OSG/SiO₂ samples. In either case, delamination requires severing of

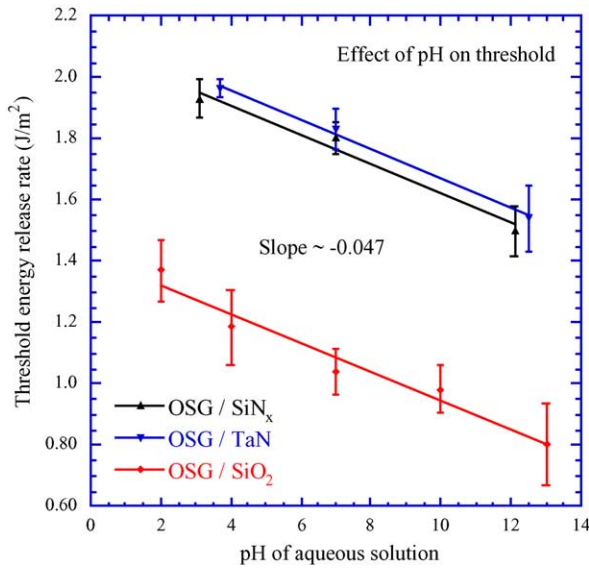


Fig. 15. Threshold energy release rate as a function of pH for delamination in aqueous environments.

Si–O bonds. It is then no surprise that the crack growth results depicted in Fig. 11 are similar for all three materials systems: crack velocity increases exponentially with applied driving force and increases with increasing water vapor pressure. These results are qualitatively similar to those obtained by Wiederhorn for bulk soda-lime glass [3] and by Lane et al. for thermally grown SiO₂ coatings [9], although the toughness of the OSG coatings is significantly lower than that of either material. This is a direct consequence of the terminal methyl groups in the OSG structure, which result in a significant reduction in the density of the material and possibly in a lower bond strength as well. The crack velocities in Fig. 11 are well represented by Eq. (10) over four orders of magnitudes of the velocity. This indicates that the crack is in the reaction-controlled regime. If one assumes that one water molecule reacts with one Si–O bond, Eq. (11) predicts that transport of water molecules to the crack tip becomes rate limiting at crack velocities in the 10⁻⁴ to 10⁻³ m/s range depending on the water partial pressure. The experimental velocities in Fig. 11 are well below this range, confirming that crack propagation is limited by reaction kinetics. In the reaction-controlled regime, the slope of the velocity data in a logarithmic plot is inversely proportional to the bond density N . As shown in Table 3, all three materials systems yield similar bond densities with an average value of (8.6 ± 2.3)

Table 3
Bond densities for each of the materials systems for fracture in both aqueous and ambient conditions

Materials system	Ambient environment (m ⁻²)	Aqueous environment (m ⁻²)
OSG/TaN	8.13×10^{18}	7.19×10^{18}
OSG/SiN _x	8.79×10^{18}	10.3×10^{18}
OSG/SiO ₂	8.87×10^{18}	6.72×10^{18}

$\times 10^{18} \text{ m}^{-2}$. This bond density is close to the value of $8.4 \times 10^{18} \text{ m}^{-2}$ one would expect based on the RBS measurements [35] and a density of 1.47 g/cm^3 for the OSG films. Values of N reported by Lane et al. for the cohesive failure of thermally grown SiO₂ coatings [9,10] are almost an order of magnitude higher.

The results for the OSG/SiO₂ samples in Fig. 13 show that at high relative humidity, the crack velocity in ambient environments is similar to that in buffer solutions with low pH. Under these humidity conditions, one needs to consider the possibility that water condenses at the crack tip to form a small pocket of water [3]. The curvature of the water meniscus is governed by the Kelvin equation [36]. If the curvature in the plane of the crack is negligible, the radius of curvature of the meniscus, ρ , is determined by

$$\ln\left(\frac{p}{p_0}\right) = \frac{\Gamma V}{\rho RT}, \quad (24)$$

where p is the vapor pressure over a surface with radius of curvature ρ , p_0 the vapor pressure over a flat surface, Γ the surface tension of water, and V is the molar volume. According to Eq. (24), the radius of curvature required for a relative humidity below 75% is smaller than 2 nm. Considering that the contact angle between water and OSG is approximately 75°, it is straightforward to show that the corresponding volume is too small to contain a significant number of water molecules and one would not expect any liquid water at the crack tip. If the relative humidity approaches 100%, however, formation of a pocket of water at the crack tip is certainly possible and the smooth transition between ambient and aqueous results in Fig. 13 is not surprising. Fig. 12 shows a linear relationship between the threshold energy release rate and the natural logarithm of the water partial pressure in the environment for the three materials systems. This behavior has been reported previously by Lane et al. [9] for subcritical fracture of amorphous silica coatings. The linear relationship can be rationalized based on Eq. (5) if the reactive species X is identified with water:

$$\begin{aligned} 2\gamma &= N(\mu_B - \mu_A - n\mu_X) \\ &= N(2\mu_{\text{Si-OH}} - \mu_{\text{Si-O-Si}} - n\mu_{\text{H}_2\text{O}}) \\ &= N(\Delta\mu - nkT \ln p_{\text{H}_2\text{O}}). \end{aligned} \quad (25)$$

Here, the equation for the chemical potential of an ideal gas was used to obtain an expression in terms of the water partial pressure. Eq. (25) indeed predicts a linear relationship between threshold and logarithm of the water partial pressure. Note that it is appropriate to include the data obtained at 100% relative humidity in Fig. 12, since the droplet that forms at the crack tip for these experiments is in equilibrium with the water vapor in the ambient, i.e., the chemical potential of the water molecules in both phases is identical. The slopes of the graphs in Fig. 12 are nearly identical for the three materials systems and can be related to the number of water molecules n involved in breaking a Si–O bond through Eq. (25). The experimental data in Fig. 12 yield a value for n of

approximately 10. This number is very close to that reported by Lane et al. [9] for amorphous silica films, but much higher than that reported by Wiederhorn [3] for bulk soda-lime glass. It is unlikely that 10 water molecules would be involved in the reaction. The high value of n was attributed by Lane et al. [9] to plastic deformation in their specimens. However, OSG/SiN_x specimens in which the thickness of the Cu layer was systematically varied from 0.1 to 2 μm, did not show any significant change in fracture toughness with increasing Cu thickness [35]. This observation combined with the fact that the slope is independent of the film stack, implies that plastic dissipation in the Cu layer does not contribute significantly to the measured energy release rates. Energy dissipation in the OSG layer as suggested by Célarié et al. [33] cannot be ruled out, but it is not clear if the effect would be large enough. Even though the linear behavior of the threshold values is consistent with the stress-corrosion model, the origin of the large slope is presently not well understood.

5.3. Effect of pH on subcritical fracture of OSG

In the reaction-controlled regime, the velocity of a crack propagating in an aqueous solution is given in Eq. (10). This equation indeed provides a good description of the experimental data in Figs. 13 and 14 over several orders of magnitude of the velocity. At large crack velocities and for large values of pH, however, the velocity curves level off and the equation tends to overestimate crack velocity. In the range where the crack velocity is reaction-controlled, the slopes of the graphs in Figs. 13 and 14 decrease slightly with increasing pH. Subcritical crack growth measurements obtained by Wiederhorn and Johnson for a range of bulk glasses [5] also suggest that the slopes of the velocity curves for these materials decrease with increasing pH of the buffer solution. This observation was attributed by these authors to a change of the crack tip radius or a change of the reaction activation volume with pH. In the model described in Section 2, a change in pH could alter the radius of curvature of the crack tip and thus affect the value of the activation area. As shown in Table 3, the values of N corresponding to the slopes of the velocity curves are similar for the three materials systems with an average value of $(8.5 \pm 1.4) \times 10^{18} \text{ m}^{-2}$, in good agreement with the ambient measurements.

Fig. 15 depicts a graph of the threshold energy release rate as a function of electrolyte pH for the three material systems. As illustrated in the figure, the threshold decreases linearly with increasing pH for the three systems. The linear behavior can again be explained by invoking Eq. (5), where the reactive species X is now identified with the hydroxyl ion:

$$\begin{aligned} 2\gamma &= N(\Delta\mu - nkT \ln a_{\text{OH}^-}) \\ &= N(\Delta\mu + 14nkT \ln 10 - nkT \ln 10 \text{ pH}), \end{aligned} \quad (26)$$

since at room temperature

$$\ln a_{\text{OH}^-} = \ln 10(\text{pH} - 14) \quad (27)$$

in an aqueous environment. The order of the reaction n can be obtained from the slope of the lines in Fig. 15 through use of Eq. (26). The value thus obtained is independent of the materials system and is equal to 0.56 ± 0.07 . This result agrees with the fractional order of 0.53 ± 0.04 observed in the dissolution experiments and suggests that both dissolution and subcritical crack growth are controlled by the same mechanism, i.e. a weakening of the Si–O bonds by chemisorption of OH[−] groups or deprotonation of Si–OH surface groups. It should be noted that this model is also consistent with recent observations by Célarié et al. [33] of the formation of cavities ahead of the crack tip in aluminosilicate glass. It is known from dissolution studies of silica glass [18] that active species can diffuse into the glass and break Si–O bonds in regions where the silica tetrahedra are weakly bonded due to atomic density fluctuations that occur naturally in amorphous silica. One could expect a similar mechanism to take place in OSG films as well.

Figs. 13 and 14 show that some of the crack velocity curves level off for velocities in the range of 10^{-6} to 10^{-5} m/s. The effect is most pronounced at high values of pH and only occurs for measurements in aqueous environment; it is absent in the ambient measurements. This is an indication that cracks in specimens tested at high pH have entered a regime where crack propagation is controlled by transport of hydroxyl ions to the crack tip. Eq. (20) predicts that the crack velocity above which flow of the aqueous solution into the crack tip becomes rate limiting is approximately 2×10^{-3} m/s, if one assumes an OSG stiffness of 12 GPa [37], a solution viscosity of 9.5×10^{-4} Pa s, a surface tension of 0.072 J/m², and a crack length of 1 mm. This value is independent of pH and well above the maximum velocity for which crack growth data were obtained. Moreover, the AFM results show that the crack faces are relatively smooth and according to Eq. (21) the reduction in the maximum velocity as a result of crack face roughness is very small. Thus, the transport of hydroxyl ions to the crack tip is not limited by fluid flow, but rather by diffusion of the hydroxyl ions in the fluid. Based on a diffusion coefficient of 5.27×10^{-5} cm²/s [38], Eq. (12) predicts a boundary layer thickness in the range of 0.1–1 μm. A diffusion-limited supply of hydroxyl ions also explains why in Fig. 14(b) all curves converge at high crack velocities: hydroxyl ions cannot keep up with the crack and crack growth becomes independent of pH.

Finally, one should also consider the possibility that the pH at the crack tip changes as the velocity increases. A decrease in pH at the crack tip reduces the crack velocity for a given driving force. This mechanism was first used by Wiederhorn and Johnson [5] to explain some of their experimental results on bulk glass and arises from an ion exchange between the glass and the electrolyte at the crack tip. Hence, the crack tip pH is controlled by the aqueous solution at low crack velocities, and by the glass composition at high velocities. This effect plays a role for materials such as soda-lime silicate glass that contain mobile alkali ions, but is not observed for silica glass. Because of its slow dissolution rate, the crack

tip pH for silica glass is controlled by the composition of the aqueous solution for velocities up to at least 10^{-4} m/s [5]. The OSG dissolution results obtained in this study demonstrate that the dissolution rate of OSG films is even slower than that of silica glass. Hence, significant changes of the pH at the crack tip due to dissolution of OSG are not likely to occur even at the highest crack velocities observed in this study.

6. Conclusions

Organosilicate glass is susceptible to subcritical crack growth due to the Si–O bonds in its structure. A dissolution study has demonstrated that OSG coatings dissolve in aqueous environments at a lower rate than silica glass and that the order of the dissolution reaction is similar to that observed for other silicates. Subcritical crack growth measurements have been performed on three materials systems, i.e., OSG/TaN, OSG/SiN_x, and OSG/SiO₂. Crack growth occurs within the OSG coating for the OSG/TaN and OSG/SiN_x systems, but at the interface for the OSG/SiO₂ system. The crack faces are quite smooth in all cases. Measurements in ambient environments are similar to previously published results for thermally grown SiO₂ coatings, although the toughness of OSG coatings is significantly lower than that of SiO₂ coatings. The presence of water vapor in the ambient results in a significant increase in crack velocity for a given energy release rate. The threshold energy release rate changes linearly with the logarithm of the water vapor pressure as predicted by the model, while the slopes of the velocity curves yield bond densities which are in line with expectations for OSG. Subcritical measurements in aqueous environments demonstrate that crack velocities increase with increasing concentration of hydroxyl ions, in agreement with the results of the dissolution study. Threshold energy release rates vary linearly with pH and suggest that both dissolution and subcritical crack growth are controlled by similar mechanisms. The bond densities obtained from the aqueous measurements are in close agreement with those obtained in the ambient measurements. At high driving forces, the crack velocity is limited by diffusion of hydroxyl ions to the crack tip.

Acknowledgements

Financial support from the Division of Engineering and Applied Sciences at Harvard University, from the

$$\Delta p = 12F\mu \int_0^l \frac{dx}{(\delta + A \sin(2\pi(y/l))[\sin(2\pi(x+\varepsilon)/l) - \sin(2\pi(x/l))])^3} = \frac{12Fl\mu}{2\pi\delta^3} \int_0^{2\pi} \frac{dt}{(1 + \eta[\sin(t+\varphi) - \sin(t)])^3}, \quad (\text{A.3})$$

Harvard MRSEC (DMR-0213805), and from the National Science Foundation (DMR-0133559; DMR-0215902) is

gratefully acknowledged. The authors also wish to thank J.A. Golovchenko for use of the dicing saw.

Appendix A. Roughness model

When crack propagation is limited by fluid flow, one would expect the roughness of the crack faces to affect the velocity of the crack. In this appendix, we present a simple model to estimate the magnitude of this effect. Consider a Cartesian coordinate system with the x -axis perpendicular to the crack front, y -axis parallel to the crack front, and z -axis perpendicular to the crack face. Assume that the average crack opening at some distance X from the crack tip is given by δ , while the relative displacement of the two crack faces with respect to each other due to the mode II loading component is represented by ε . Assume further that the crack face is well described by a sinusoidal function of amplitude A , where A is a measure of the roughness of the crack. The width of the channel available for fluid flow is then

$$h(x, y) = \delta + A \sin\left(2\pi\frac{y}{l}\right) \left[\sin\left(2\pi\frac{x+\varepsilon}{l}\right) - \sin\left(2\pi\frac{x}{l}\right) \right], \quad (\text{A.1})$$

where l is the characteristic wavelength of the roughness. For a crack loaded in mode I, ε is zero and the width of the channel remains constant since the topography of both crack faces is identical. This is of course only true if plastic deformation at the crack tip is negligible. If the loading has a mode II component, the channel width varies in both x and y -directions. Since the Reynolds number for this system approaches zero, fluid flow through the channel is laminar and it follows that

$$\frac{dp}{dx} = \frac{12F\mu}{h^3}, \quad (\text{A.2})$$

where p is the pressure, μ the viscosity of the fluid, and F the flow through the channel per unit width in the y -direction. Note that implicit to Eq. (A.2) is the assumption that the flow pattern is one-dimensional, i.e., flow occurs in the x -direction only. As a result, F is independent of x , but is a function of y since the width of the channel is modulated in this direction. The crack opening displacement δ generally varies very little over one wavelength of the roughness and can therefore be regarded as constant at this length scale. Integrating Eq. (A.2) over one wavelength in the x -direction provides the corresponding pressure drop

after substituting $t = 2\pi x/l$, $\varphi = 2\pi\varepsilon/l$, and

$$\eta = \frac{A}{\delta} \sin\left(2\pi\frac{y}{l}\right). \quad (\text{A.4})$$

After some manipulations, the integral in Eq. (A.3) can be readily calculated to yield

$$\Delta p = \frac{12Fl\mu}{\delta^3} \frac{1 + \eta^2(1 - \cos \varphi)}{(1 - 2\eta^2(1 - \cos \varphi))^{5/2}}. \quad (\text{A.5})$$

The flow per unit width averaged in the y -direction is

$$\begin{aligned} \bar{F} &= \frac{1}{l} \int_0^l F \, dy = \frac{\Delta p \delta^3}{12\mu l^2} \int_0^l \frac{(1 - 2\eta^2(1 - \cos \varphi))^{5/2}}{1 + \eta^2(1 - \cos \varphi)} \, dy \\ &= \frac{\Delta p \delta^3}{24\pi\mu l} \int_0^{2\pi} \frac{(1 - 2\lambda \sin^2 \zeta)^{5/2}}{1 + \lambda \sin^2 \zeta} \, d\zeta = \frac{\Delta p \delta^3}{12\mu l} \rho(\lambda), \end{aligned} \quad (\text{A.6})$$

where

$$\lambda = \left(1 - \cos \frac{2\pi\varepsilon}{l}\right) \left(\frac{A}{\delta}\right)^2 \quad (\text{A.7})$$

and

$$\rho(\lambda) = \frac{1}{2\pi} \int_0^{2\pi} \frac{(1 - 2\lambda \sin^2 \zeta)^{5/2}}{1 + \lambda \sin^2 \zeta} \, d\zeta. \quad (\text{A.8})$$

Rewriting Eq. (A.6) as follows:

$$\frac{\Delta p}{l} = \frac{1}{\rho(\lambda)} \frac{12\bar{F}\mu}{\delta^3}, \quad (\text{A.9})$$

and comparing with Eq. (A.2) shows that $\rho(\lambda)$ is a simple correction factor that captures the effect of the roughness of the crack faces. Note that Eq. (A.8) requires that $2\lambda \sin^2 \zeta \leq 1$, i.e., asperities from both crack faces should not interpenetrate. In actual reality, asperities do not interpenetrate, but deform elastically or plastically pinching off the channel. Hence, the integrand in Eq. (A.8) can be taken equal to zero whenever $2\lambda \sin^2 \zeta > 1$. In a simple one-dimensional model, fluid flow to the crack tip would be stopped completely in this case; in the two-dimensional model discussed here, however, there are channels available for the fluid to reach the crack tip. Fig. A.1 shows the correction factor $\rho(\lambda)$ as a function of λ . As expected, the correction factor is equal to one for perfectly smooth crack faces and decreases slowly with increasing roughness.

Since l is often small compared to the crack length – l is approximately 30–40 nm in the present study, the left hand side of Eq. (A.9) is in effect the derivative of the pressure with respect to x . Note the similarity between Eqs. (A.2) and (A.9). As long as the correction factor $\rho(\lambda)$ is taken into account and the average channel width is used, flow through a rough crack is described by exactly the same equation as flow in a smooth channel.

Using Eq. (A.9) instead of Eq. (A.2), Eq. (15) can be rewritten as

$$\frac{dp}{dx} = \frac{1}{\rho(\lambda)} \frac{3F\mu}{2u^3} = \frac{3\pi\mu v_3 E}{8G(1 - \nu^2)} \frac{1}{x\rho(\lambda)}. \quad (\text{A.10})$$

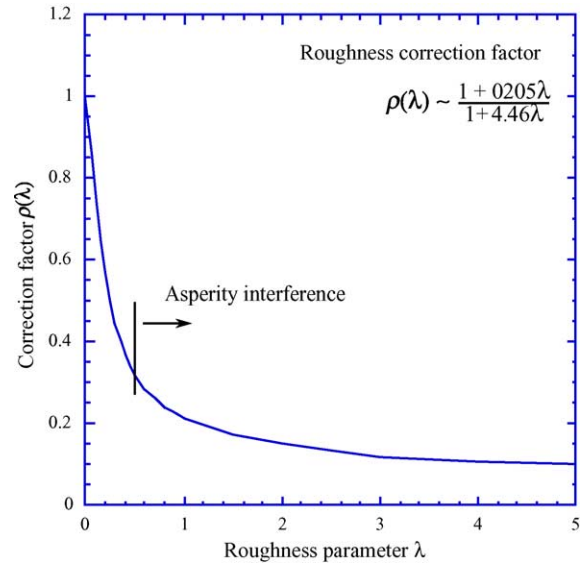


Fig. A.1. Correction factor $\rho(\lambda)$ as a function of the roughness parameter λ .

Integration of this equation results in

$$p(x) = p_a - \frac{3\pi\mu v_3 E}{8G(1 - \nu^2)} \int_x^c \frac{1}{x\rho(\lambda)} \, dx, \quad (\text{A.11})$$

which is identical to Eq. (21). The integral in Eq. (A.11) needs to be evaluated numerically. Near the crack tip, λ can be expanded in a Taylor series:

$$\lambda \approx 2\pi^2 \left(\frac{A}{l}\right)^2 \left(\frac{\varepsilon}{\delta}\right)^2 = 2\pi^2 \left(\frac{A}{l}\right)^2 \tan^2 \psi, \quad (\text{A.12})$$

where ψ is the loading phase angle. Since the effect of roughness is most pronounced near the crack tip where the channel is narrow, this equation shows that the relative amplitude of the roughness and the mode mix are the most relevant parameters affecting the flow. For the samples in this investigation, the effect of roughness on crack velocity is small. According to Eq. (A.11), the limiting velocity would be reduced by only a few percent due to the roughness of the crack faces. If the amplitude of the roughness was on the order of 10 nm instead of 1 nm, however, the crack velocity would be reduced by a factor of two or three. Note that if the roughness of the crack faces is due to void formation and plastic deformation as suggested by Célarié et al. [33], the profile assumed in Eq. (A.1) does not apply, although one would again expect the correction factor to be relatively small.

References

- [1] R.F. Cook, E.G. Liniger, J. Am. Ceram. Soc. (1993) 76.
- [2] B.R. Lawn, Mater. Sci. Eng. 13 (1974) 277–283.
- [3] S.M. Wiederhorn, J. Am. Ceram. Soc. 50 (1967) 407–415.
- [4] S.M. Wiederhorn, L.H. Bolz, J. Am. Ceram. Soc. 53 (1970) 543–548.
- [5] S.M. Wiederhorn, H. Johnson, J. Am. Ceram. Soc. 56 (1973) 192–197.

- [6] S.M. Wiederhorn, E.R. Fuller Jr., R. Thomson, *Metal Sci.* 14 (1980) 450–458.
- [7] R.F. Cook, E.G. Liniger, *J. Electrochem. Soc.* 146 (1999) 4439–4448.
- [8] S.-Y. Kook, R. Dauskardt, *J. Appl. Phys.* 91 (2002) 1293–1303.
- [9] M. Lane, R. Dauskardt, Q. Ma, H. Fujimoto, N. Krishna, *Proceedings of the Materials Research Society, San Francisco, CA, 1999*, pp. 251–256.
- [10] M.W. Lane, J.M. Snodgrass, R.H. Dauskardt, *Microelectron. Reliab.* 41 (2001) 1615–1624.
- [11] Y. Lin, J.J. Vlassak, T.Y. Tsui, A.J. McKerrow, *Proceedings of the Materials Research Symposium, San Francisco, CA, 2003*, p. 766.
- [12] Y. Lin, J.J. Vlassak, T.Y. Tsui, A.J. McKerrow, *Proceedings of the Materials Research Symposium, Boston, MA, 2004*, pp. 93–98.
- [13] P.E. Guyer, R. Dauskardt, *Nature Mater.* 3 (2004) 53–57.
- [14] B.V. Brady, J.V. Walther, *Geochim. Cosmochim. Acta* 53 (1989) 2823–2830.
- [15] B.R. Lawn, *J. Mater. Sci.* 10 (1975) 469–480.
- [16] T.A. Michalske, S.W. Freiman, *Nature* 295 (1982) 511–512.
- [17] R.K. Iler, *The Chemistry of Silica: Solubility, Polymerization, Colloid and Surface Properties, and Biochemistry*, Wiley, New York, 1979.
- [18] J.J. Mazer, J.V. Walther, *J. Non-Cryst. Solids* 170 (1994) 32–45.
- [19] J.D. Rimstidt, H.L. Barnes, *Geochim. Cosmochim. Acta* 44 (1980) 1683–1699.
- [20] B.V. Brady, J.V. Walther, *Chem. Geol.* 82 (1990) 253.
- [21] G. Furrer, W. Stumm, *Geochim. Cosmochim. Acta* 50 (1986) 1847–1860.
- [22] W.B. Hillig, R.J. Charles, Surfaces, stress-dependent surface reactions, and strength, in: V.F. Zackey (Ed.), *Proceedings of the Second Berkeley International Materials Conference on High-Strength Materials – Present Status and Anticipated Developments*, Wiley, 1965, pp. 682–705.
- [23] S.M. Wiederhorn, P.R. Townsend, *J. Am. Ceram. Soc.* 53 (1970) 486.
- [24] J.R. Rice, *J. Mech. Phys. Solids* 26 (1978) 61–78.
- [25] T.A. Michalske, V.D. Frechette, *J. Am. Ceram. Soc.* 63 (1980) 603–609.
- [26] M.F. Kanninen, C.H. Popelar, *Advanced Fracture Mechanics*, Oxford University Press, New York, 1985.
- [27] P.G. de Gennes, *Rev. Modern Phys.* 57 (1985) 827–863.
- [28] T.Y. Tsui, R. Willecke, A.J. McKerrow, *Proceedings of the IEEE International Interconnect Technology Conference, Burlingame, CA, 2003*, pp. 45–47.
- [29] P.G. Charalambides, J. Lund, A.G. Evans, R.M. McMeeking, *Trans. ASME, J. Appl. Mech.* 56 (1989) 77–82.
- [30] P.G. Charalambides, H.C. Cao, J. Lund, A.G. Evans, *Mech. Mater.* 8 (1990) 269–283.
- [31] J.W. Hutchinson, Z. Suo, *Adv. Appl. Mech.* 29 (1991) 63–191.
- [32] Q. Ma, *J. Mater. Res.* 12 (1997) 840–845.
- [33] F. Célarié, S. Prades, D. Bonamy, L. Ferrero, E. Bouchaud, C. Guillot, C. Marlière, *Phys. Rev. Lett.* 90 (2003) 075501–075504.
- [34] G. Wirth, J. Gieskes, *J. Colloid Interf. Sci.* 68 (1979) 492–500.
- [35] Y. Lin, J.J. Vlassak, *Unpublished results*, 2004.
- [36] W. Thomson, *Philos. Mag.* 42 (1871) 448–452.
- [37] Y. Xiang, T.Y. Tsui, J.J. Vlassak, A.J. McKerrow, *IITC Proc.* (2003).
- [38] CRC, *Handbook of Chemistry and Physics*, CRC Press LLC, Boca Raton, FL, 2003–2004.